DEUTSCHES ELEKTRONEN-SYNCHROTRON DESY

DESY 86-004
February 1986

TRIANGULAR DISCRETIZATION METHOD FOR THE EVALUATION OF RF-FIELDS IN WAVEGUIDES AND CYLINDRICALLY SYMMETRIC CAVITIES

by

U. van Rienen, T. Weiland

Deutsches Elektronen-Synchrotron DESY, Hamburg

ISSN 0418-9833

NOTKESTRASSE 85 · 2 HAMBURG 52

To be sure that your preprints are promptly included in the HIGH ENERGY PHYSICS INDEX send them to the following address (if possible by air mail) :

DESY
Bibliothek
Notkestrasse 85
2 Hamburg 52
Germany

DESY 86-004
January 1986

ISSN 0418-9833

Triangular Discretization Method for the Evaluation of RF-Fields in Waveguides and Cylindrically Symmetric Cavities

U. VAN RIENEN AND T. WEILAND

ABSTRACT. The design of rf accelerating structures nowadays is largely based on mesh-codes that solve for fields and eigenfrequencies in arbitrarily shaped cavities. The most developed codes deal with structures of cylindrical symmetry. However, no program is available that can solve for fields with azimuthal variation in cavities with dielectric and/or permeable insertions.

Here we describe a discretization method using an "orthogonal triangular double grid". The special mesh and the FIT-discretization [**11**] enable the treatment of cavities and waveguides with arbitrary material insertions and combines the features of SUPERFISH [**2**] (triangular mesh, rotationally symmetric fields) and URMEL [**9**], [**12**] (rectangular mesh but fields with or without azimuthal variation).

1. INTRODUCTION

1.1 Cylindrical Cavities. In cavities of cylindrical symmetry the electromagnetic fields are periodic in the azimuthal variable (φ) with period 2π. This fact and the harmonic time dependence of the fields allow their description by a Fourier series:

$$\begin{aligned}\vec{F}(r,\varphi,z,t) = \sum_{m=0}^{\infty} \mathrm{Re}\,\{\{ \quad & \underline{F}_r(r,z)e^{im\varphi}\vec{e}_r \\ & +\underline{F}_\varphi(r,z)e^{im\varphi}\vec{e}_\varphi \\ & +\underline{F}_z(r,z)e^{im\varphi}\vec{e}_z\} \quad e^{i\omega t}\}\end{aligned} \tag{1}$$

with the complex magnitude $\underline{\vec{F}} = \underline{\vec{E}}$ or $\underline{\vec{H}}$ and the unit vectors $\vec{e}_r$, $\vec{e}_\varphi$, $\vec{e}_z$ in r,φ,z direction. Furthermore the materials are assumed loss free, i.e. ϵ, μ are real and the conductivity is equal to zero.
So we may write

$$\begin{aligned}\vec{E} &= \sqrt{Z_0}\sin\omega t\vec{E}' \\ \vec{H} &= \sqrt{Y_0}\cos\omega t\vec{H}'\end{aligned} \tag{2}$$

with $Z_0 = \sqrt{\mu_0/\epsilon_0}$, $Y_0 = \sqrt{\epsilon_0/\mu_0}$, $c = 1/\sqrt{\mu_0\epsilon_0}$.

Then Maxwell's equations are given by

$$\begin{aligned}\mathrm{curl}\ \vec{H}' &= \epsilon_r\frac{\omega}{c}\vec{E}' \\ \mathrm{curl}\ \vec{E}' &= \mu_r\frac{\omega}{c}\vec{H}'\end{aligned} \tag{3}$$

The azimuthal dependence $e^{im\varphi}$ leads to several groups of modes:
$m = 0$: "TE-" or "H-"modes with $\vec{E} = (0, E_\varphi, 0)$
$m = 0$: "TM-" or "E-"modes with $\vec{H} = (0, H_\varphi, 0)$ (accelerating modes)
$m > 0$: these so called deflecting or transverse modes are excited by off-axis particles

1.2 Waveguides. In waveguides which don't change their characteristics in the z-direction, using cartesian coordinates, waves with pure exponential dependence of z are proper solutions of Maxwell's equations. Consequently we may write for waves travelling in the negative z-direction

$$\begin{aligned}\vec{F}(x,y,z,t) = \mathrm{Re}\,\{\{ \quad & \underline{F}_x(x,y)e^{i\beta z}\vec{e}_x \\ & +\underline{F}_y(x,y)e^{i\beta z}\vec{e}_y \\ & +\underline{F}_z(x,y)e^{i\beta z}\vec{e}_z\} \quad e^{i\omega t}\}\end{aligned} \tag{4}$$

with the complex magnitude $\underline{\vec{F}} = \underline{\vec{E}}$ or $\underline{\vec{H}}$ and the cartesian unit vectors $\vec{e}_x$, $\vec{e}_y$, $\vec{e}_z$.

With

$$\vec{E} = \sqrt{Z_0} \sin \omega t \vec{E}'$$
$$\vec{H} = \sqrt{Y_0} \cos \omega t \vec{H}' \tag{5}$$

we get for Maxwell's equations

$$\text{curl } \vec{H}' = \epsilon_r \frac{\omega}{c} \vec{E}'$$
$$\text{curl } \vec{E}' = \mu_r \frac{\omega}{c} \vec{H}' \tag{6}$$

2. DISCRETIZATION

Because of the cylindrical symmetry of the cavity (respectively the z-independence of the waveguide shape), a two dimensional grid is sufficient. As we will see the azimuthal dependence or else the z-dependence of the fields can be taken out of the numerical computation (compare [**9**], [**10**],[**11**]).

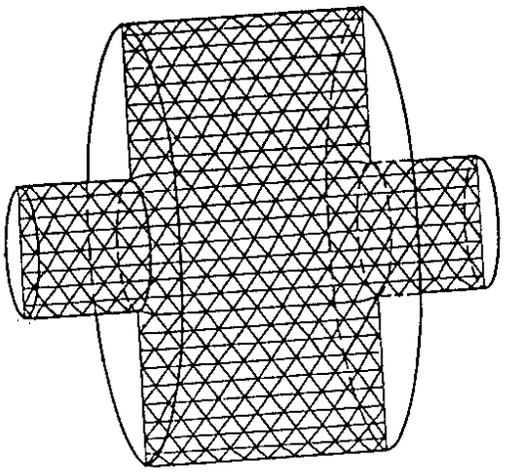

Figure 1 Pillbox cavity with triangular mesh

The basic ideas of the FIT-method have been transferred to a triangular mesh. This mesh has the advantage of approximating well the cavity or waveguide geometry even for elliptical or circular structures with relatively coarse grids.

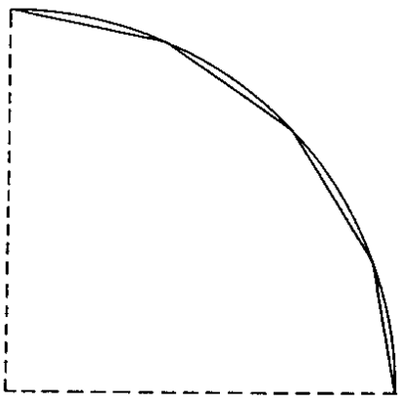

Figure 2
Approximation with a triangular mesh
(N = 16 mesh points)

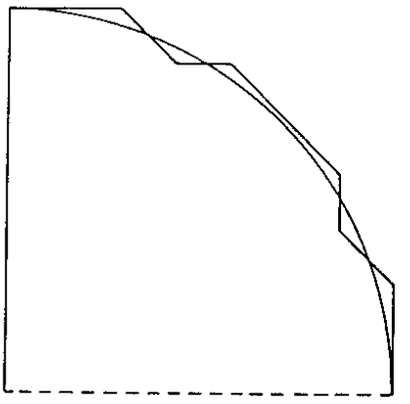

Figure 3
Approximation with a rectangular mesh using also diagonals
(N = 64 mesh points)

2.1 Allocation of the field components to the grid. In the rectangular mesh of URMEL the field components E_r, E_φ, E_z of $\vec{E}'$ and H_r, H_φ, H_z of $\vec{H}'$ (respectively E_x, E_y, E_z of $\vec{E}'$ and H_x, H_y, H_z of $\vec{H}'$) are represented as shown in figure 4 [9] .

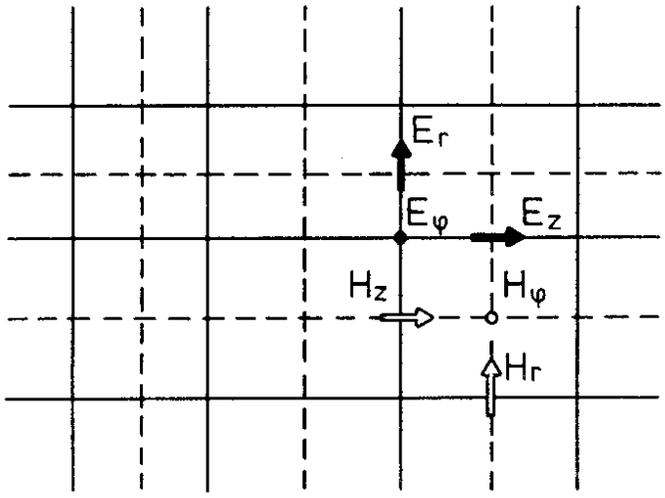

Figure 4 Rectangular mesh and its dual mesh with E_r, E_φ, E_z and H_r, H_φ, H_z

Two dual grids are used - one for the electric and one for the magnetic field components. Different components associated with one mesh point are allocated at different locations of the grid. The characteristic and the advantage of this allocation is the preservation of the interrelation between the integrals over areas and the line integrals in Maxwell's equations. For the triangular mesh we proceed in full analogy.

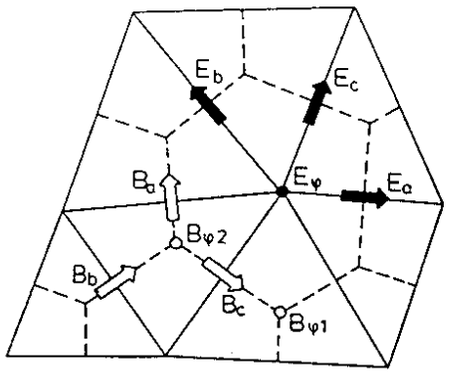

Figure 5
Triangular mesh and its dual (hexagonal) mesh with E_a, E_b, E_c, E_φ and B_a, B_b, B_c, B_{φ_1}, B_{φ_2}

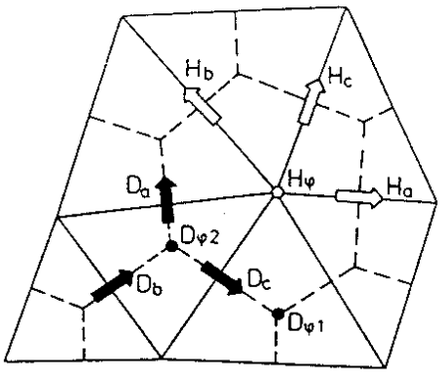

Figure 6
Triangular mesh with dual mesh and H_a, H_b, H_c, H_φ, D_a, D_b, D_c, D_{φ_1}, D_{φ_2}

But here we have to distinguish two cases:

(1) If all triangles of the mesh inside the cavity have angles less than or equal to $\pi/2$ we choose as dual mesh lines the perpendicular bisectors of the sides (see figures 5

and 6). These intersect in the center of a circle drawn through the three vertices of the triangle.

(2) The program starts with a mesh of regular triangles and varies it in order to approximate the given boundaries as well as possible. In this process it can not always avoid triangles with an angle over $\pi/2$.
If this happens the use of the above-defined dual mesh points would lead to the following problem: Some dual mesh points are outside the proper triangles.
In this case we use the centres of mass as dual mesh points.
It should be noted that the $\tilde{\vec{F}}$ -component in this dual mesh is in general not perpendicular to the $\vec{F}$-component (see figure 8).

In the following we will denote the dual mesh with perpendicular bisectors for sides as $\mathbf{G_M}$, that with centres of mass as $\mathbf{G_S}$ and the triangular mesh as $\mathbf{G}$.

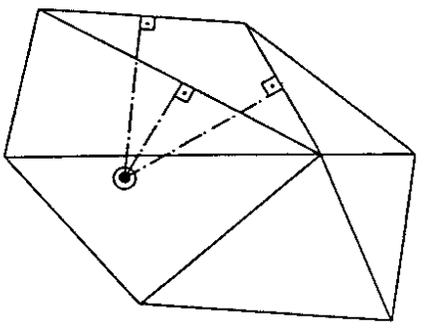

Figure 7
For flat triangles the center of the circumscribed circle lies outside

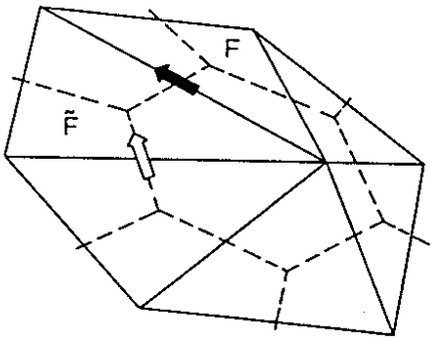

Figure 8
Dual mesh with centres of mass as mesh points; (F,$\tilde{\text{F}}$)=(E,B) or (H,D)

The numbering of mesh points and the allocation of the triangles to these points is explained in the following. The numbering of the mesh points is done analogously to URMEL as may be seen in figure 9. This picture also demonstrates that there are two kinds of triangles alternating in the rows: one has the vertex on top while the other one is standing upright. One of each kind is associated to each mesh point k ($k = (j-1)\cdot J + i$ with $j = 1, ..., J, i = 1, ..., I$). The triangle of the first kind is named $(1, k)$ and the second $(2, k)$. As figure 9 demonstrates the order of the triangles starts with one of the first kind in the rows with an odd number (j) and with one of the second kind in all rows with an even number (j).
Figure 10 shows for a general mesh point k all adjacent triangles, triangle-sides and mesh points. Evidently a part of this is nil for boundary points.
In some places in the formulas, following here and in the appendix, superposed indices are used. The upper one always refers to the formula for a point $k = (j-1)\cdot J + i$ in row j with even j (type I) , while the lower one refers to the formula for k in row j with odd j (type II). The allocation of the all field components, associated to a mesh point, is illustrated in figure 11 for the points l of the type I and k of type II.

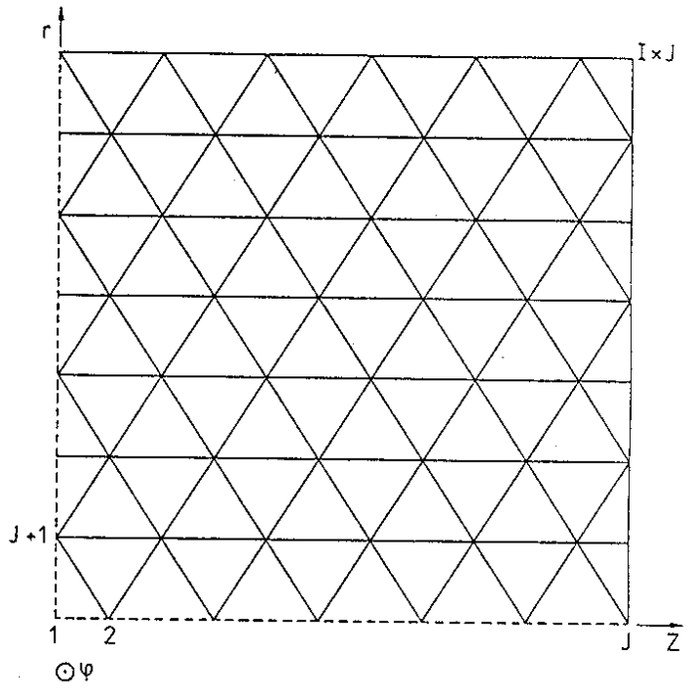

Figure 9 Numbering of the mesh points

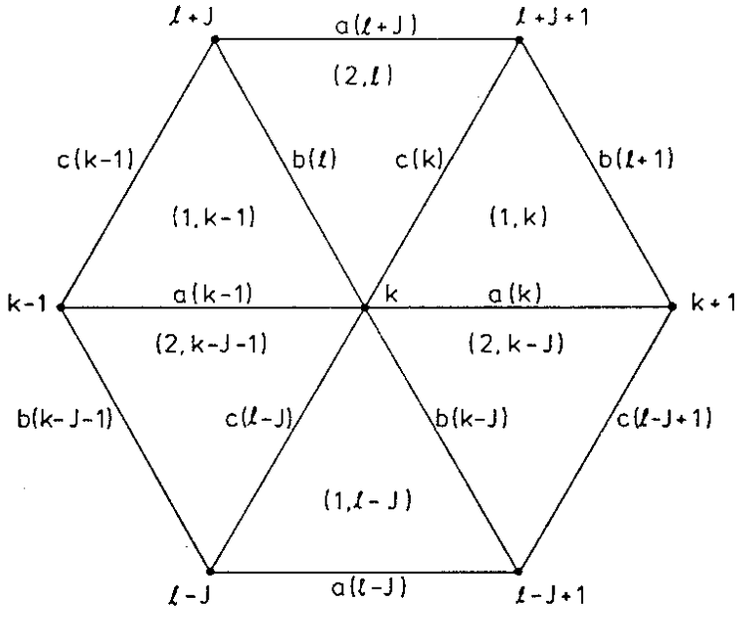

with $k = (j-1)\cdot J + i$

and $\ell = \begin{Bmatrix} k \\ k-1 \end{Bmatrix}$ for $\begin{Bmatrix} j & \text{even} \\ j & \text{odd} \end{Bmatrix}$

Figure 10 Points, sides and triangles adjacent to a mesh point

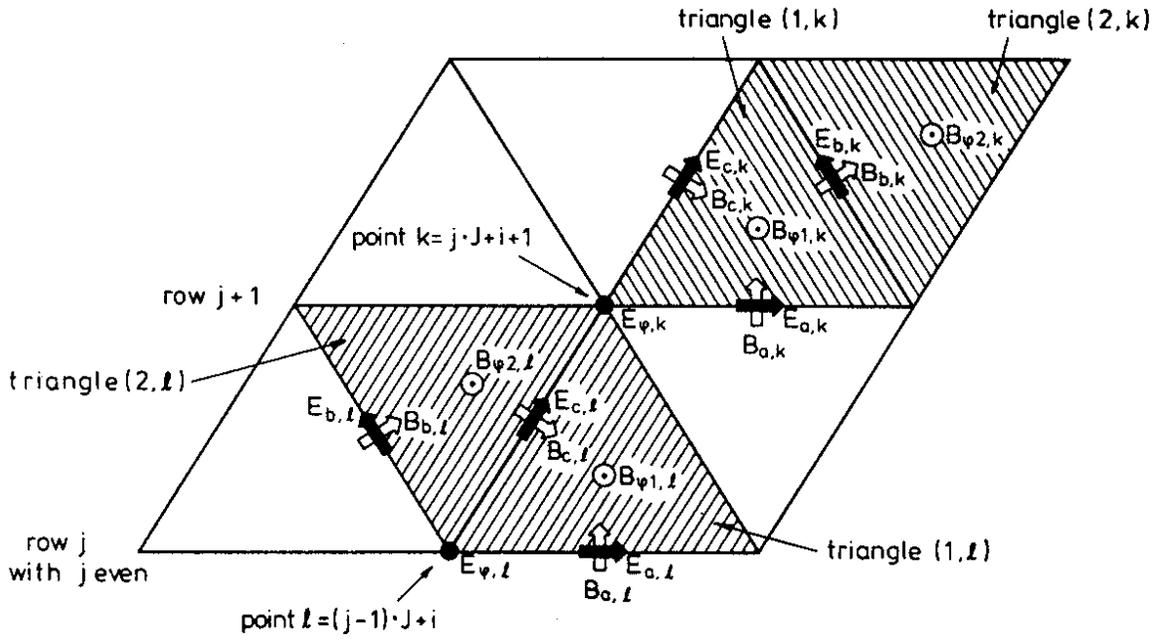

Figure 11 Location of the field components and the triangles associated with one mesh point

2.2 Allowed material properties in the different grids. As mentioned above, the permittivity and the permeability shall be real. For $\mathbf{G_M}$ as dual mesh any inserted material may have $\mu_r \neq 1$ *and* $\epsilon_r \neq 1$ and either E or H could be chosen for F(see figures 12 and 13). In figure 12 it may be seen that only continuous components (i.e. tangential E and normal B) occur so that triangles of **G** may be filled with materials with $\mu_r \neq 1$ and $\epsilon_r \neq 1$ and varying from triangle to triangle. Similarly in figure 13 only tangential H and normal D occur at the triangle boundaries.

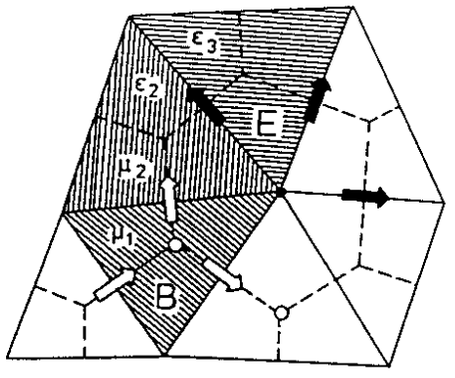

Figure 12
E on **G**, B on $\mathbf{G_M}$, $\mu_r \neq 1$, $\epsilon_r \neq 1$

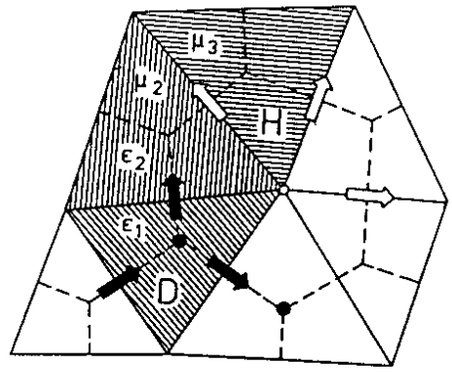

Figure 13
H on **G**, D on $\mathbf{G_M}$, $\mu_r \neq 1$, $\epsilon_r \neq 1$

If only the dual mesh $\mathbf{G_S}$ can be used we have to place a restriction to assure the continuity of the field components: Only insertions with $\mu_r \neq 1$ but $\epsilon_r = 1$ or $\epsilon_r \neq 1$ but

$\mu_r = 1$ are allowed and F will be taken as shown in figures 14 and 15. In figure 14 it is seen that (continuous) tangential E occurs at the triangle interfaces, and so ϵ_r can vary from triangle to triangle. However since on the dual mesh the magnetic field component is not normal to the interfaces, μ_r can not vary from triangle to triangle . Similarly, in figure 15 it can be seen that, with H on the mesh **G**, μ_r can vary whereas ϵ_r cannot.

Although the constants μ_0 and ϵ_0 are shown in figure 14 and 15, in fact if the cavity or waveguide were completely filled with a medium with constant μ_r or constant ϵ_r, respectively, only continuous field components would occur.

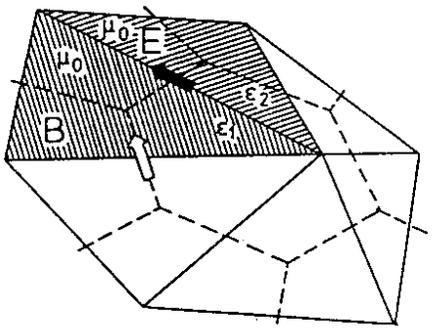

Figure 14
E on **G**, B on $\mathbf{G_S}$, $\mu = \mu_0$, $\epsilon_r \neq 1$

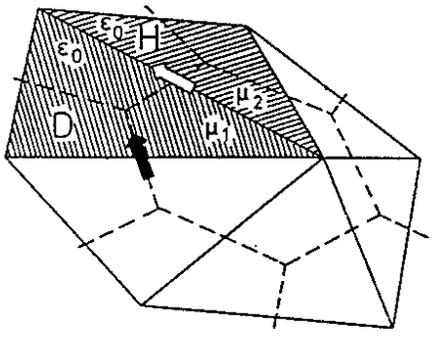

Figure 15
H on **G**, D on $\mathbf{G_S}$, $\mu_r \neq 1$, $\epsilon = \epsilon_0$

However for nearly all structures it is possible to find a mesh which renders $\mathbf{G_M}$ possible as dual mesh.

2.3 Deflecting modes, $m > 0$. On the given presumptions the electromagnetic fields can be written as:

$$\begin{aligned}\vec{E}(r,\varphi,z,t) = &\sqrt{Z_0}\sin\omega t \quad \sum_{m=0}^{\infty}\{ \quad E_{m,r}(r,z)\cos m\varphi\ \vec{e}_r \\ &+ \quad E_{m,\varphi}(r,z)\sin m\varphi\ \vec{e}_\varphi \\ &+ \quad E_{m,z}(r,z)\cos m\varphi\ \vec{e}_z \quad \} \end{aligned} \tag{7}$$

$$\begin{aligned}\vec{H}(r,\varphi,z,t) = &\sqrt{Y_0}\cos\omega t \quad \sum_{m=0}^{\infty}\{ \quad H_{m,r}(r,z)\sin m\varphi\ \vec{e}_r \\ &+ \quad H_{m,\varphi}(r,z)\cos m\varphi\ \vec{e}_\varphi \\ &+ \quad H_{m,z}(r,z)\sin m\varphi\ \vec{e}_z \quad \} \end{aligned} \tag{8}$$

As in (2) we will use $\vec{E}'$ and $\vec{H}'$. For $(\vec{F}',\vec{\tilde{F}}') = (\vec{H}',\vec{D}')$ we choose $\varphi = \varphi + \pi/2$ in (7) and (8). For each azimuthal mode number m Maxwell's equations in integral form read then as:

$$\begin{aligned}\oint \vec{H}'\cdot d\vec{s} &= \frac{\omega}{c}\int \epsilon_r\vec{E}'\cdot d\vec{A} \\ \oint \vec{E}'\cdot d\vec{s} &= \frac{\omega}{c}\int \mu_r\vec{H}'\cdot d\vec{A} \\ \iint \epsilon_r\vec{E}'\cdot d\vec{A} &= 0 \\ \iint \mu_r\vec{H}'\cdot d\vec{A} &= 0 \end{aligned} \tag{9}$$

These equations are solved for a chosen $m > 0$ in the following way:

- They are discretized on the triangular mesh $\mathbf{G}$ with $\mathbf{G_S}$ (respectively $\mathbf{G_M}$) for $(\vec{F}',\vec{\tilde{F}}')=(\vec{E}',\vec{B}')$ or $(\vec{H}',\vec{D}')$. The boundary conditions are implied in the discretization. The details are given in the appendix.

- In the resulting equations all $\vec{\tilde{F}}'$-components and the azimuthal $\vec{F}'$-component F_φ are eliminated.
  This leads to a linear algebraic eigenvalue problem connecting each field component F_a, F_b, F_c with ten neighbours :

$$\begin{aligned}\left(\tfrac{\omega}{c}\right)^2 F_{a,k} = \quad & \alpha_{aa,k,0}F_{a,k} \\ &+ \alpha_{aa,k,1}F_{a,k+1} + \alpha_{aa,k,2}F_{a,k-1} \\ &+ \alpha_{ab,k,0}F_{b,k} + \alpha_{ab,k,1}F_{b,k\pm1} \\ &+ \alpha_{ab,k,2}F_{b,k-J+1} + \alpha_{ab,k,3}F_{b,k-J} \\ &+ \alpha_{ac,k,0}F_{c,k} + \alpha_{ac,k,1}F_{c,k+1} \\ &+ \alpha_{ac,k,2}F_{c,k-J\pm1} + \alpha_{ac,k,3}F_{c,k-J} \end{aligned} \tag{10}$$

$$\begin{aligned}\left(\tfrac{\omega}{c}\right)^2 F_{b,k} = \quad & \alpha_{bb,k,0}F_{b,k} \\ &+ \alpha_{bb,k,1}F_{b,\,k+J-1\ \ k+J} + \alpha_{bb,k,2}F_{b,\,k-J\ \ k-J+1} \\ &+ \alpha_{ba,k,0}F_{a,k} + \alpha_{ba,k,1}F_{a,k+J} \\ &+ \alpha_{ba,k,2}F_{a,k+J-1} + \alpha_{ba,k,3}F_{a,k\mp1} \\ &+ \alpha_{bc,k,0}F_{c,k} + \alpha_{bc,k,1}F_{c,k+J} \\ &+ \alpha_{bc,k,2}F_{c,k\mp1} + \alpha_{bc,k,3}F_{c,k-J} \end{aligned} \tag{11}$$

$$
\begin{aligned}
\left(\tfrac{\omega}{c}\right)^2 F_{c,k} = \quad & \alpha_{cc,k,0} F_{c,k} \\
& + \alpha_{cc,k,1} F_{c,\,{}^{k+J+1}_{k+J}} + \alpha_{cc,k,2} F_{c,\,{}^{k-J}_{k-J-1}} \\
& + \alpha_{ca,k,0} F_{a,k} + \alpha_{ca,k,1} F_{a,k+J\pm 1} \\
& + \alpha_{ca,k,2} F_{a,k+J} + \alpha_{ca,k,3} F_{a,k-1} \\
& + \alpha_{cb,k,0} F_{b,k} + \alpha_{cb,k,1} F_{b,k+J} \\
& + \alpha_{cb,k,2} F_{b,k\pm 1} + \alpha_{cb,k,3} F_{b,k-J}
\end{aligned}
\tag{12}
$$

This relation between the field components is schematically illustrated in figure 16.

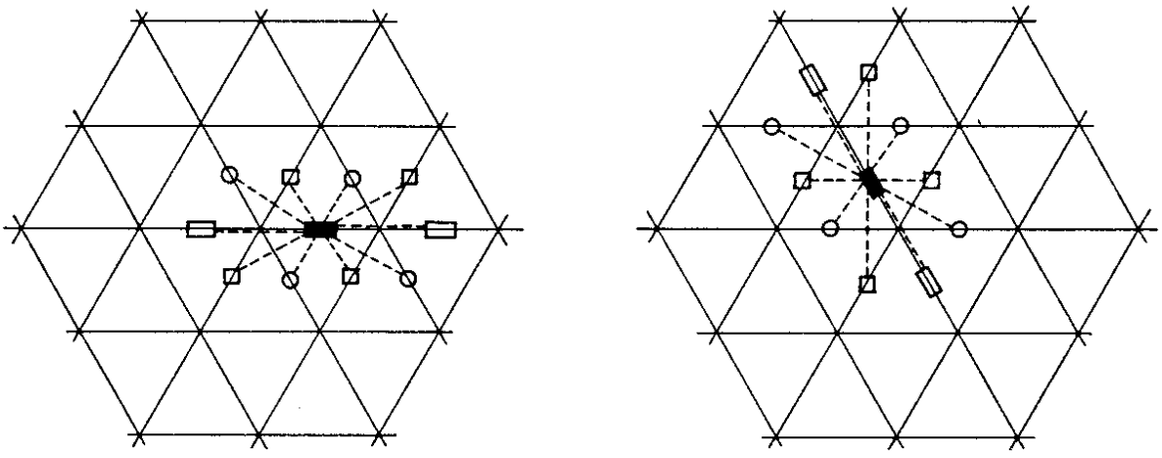

Figure 16 Illustration of the connection to ten neighbours by the difference equations for $F_{a,k}$ and $F_{b,k}$

The equations (10)-(12) which are given for every mesh point k correspond in their matrix representation to a linear algebraic eigenvalue problem. Thus an eigenvalue problem

$$
A\vec{x} = k^2 \vec{x} \qquad \text{with the wave number} \quad k = \frac{\omega}{c} \tag{13}
$$

remains to be solved. Its eigenvalues are the squared wave numbers of the resonant frequencies and the eigenvectors

$$
\vec{x} = (F_{a,1}, \ldots, F_{a,N}, F_{b,1}, \ldots, F_{b,N}, F_{c,1}, \ldots, F_{c,N})^T
$$

give the corresponding electric and magnetic fields. Here an advantage of the FIT-method becomes obvious: While other methods (e.g. SUPERFISH [**2**], PRUD [**1**]) don't solve a linear problem and need an estimation of the frequency sought this method solves a linear problem of which the solution gives the resonant frequencies.
Since pure TE- and TM-modes (see section 2.4) exist as deflecting modes only for the pillbox cavity all six field components have to be calculated.

$$\begin{pmatrix} A_{aa} & A_{ab} & A_{ac} \\ A_{ba} & A_{bb} & A_{bc} \\ A_{ca} & A_{cb} & A_{cc} \end{pmatrix}$$

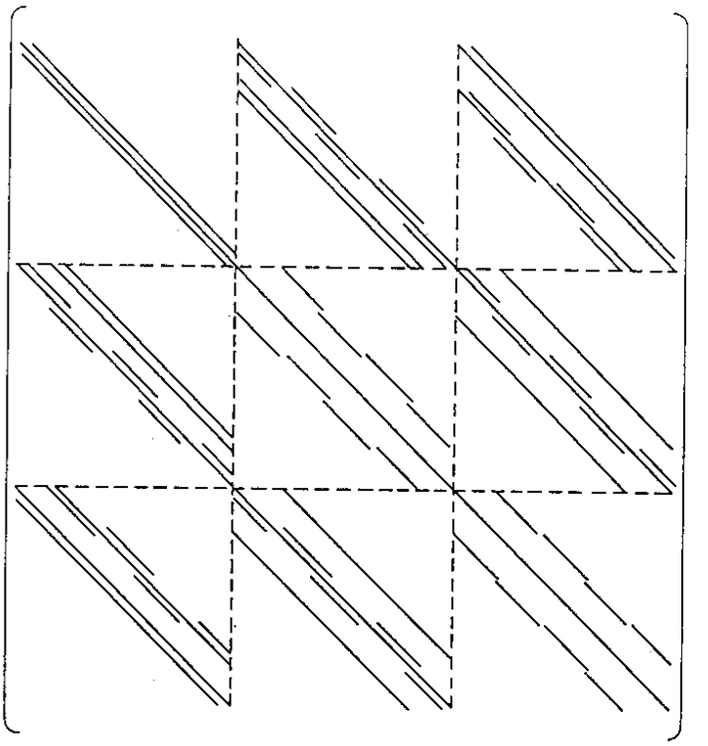

Figure 17 Matrix of the eigenvalue problem for $m > 0$

The matrix of the eigenvalue problem is sparse and the non-zero elements lie on a few off-diagonals as shown in figure 17. The matrix is 3N x 3N.

2.4 Monopole modes, $m = 0$. Here we have to distinguish two classes of modes:

TE0-modes	transversal electric fields with $E_z = 0$;
	$E_r = 0$, $H_\varphi = 0$, H_r, H_z and E_φ have to be calculated.
TM0-modes	transversal-magnetic fields with $H_z = 0$;
	$H_r = 0$, $E_\varphi = 0$, E_r, E_z and H_φ are calculated.

Maxwell's equations (9) are solved for m=0 as follows:

- They are discretized on the triangular mesh with $(\vec{F}', \tilde{\vec{F}}')=(\vec{E}', \vec{B}')$ for TM-modes and $(\vec{F}', \tilde{\vec{F}}')=(\vec{H}', \vec{D}')$ for TE-modes. (See appendix for details)
- In the resulting equations all $\vec{F}'$-components are eliminated . $\tilde{F}_{\varphi 1}$ and $\tilde{F}_{\varphi 2}$ are the only non-zero $\tilde{\vec{F}}'$-components.
  Again we obtain a linear eigenvalue problem - in this case connecting each field component $\tilde{F}_{\varphi 1}$ and $\tilde{F}_{\varphi 2}$ with three neighbours:

$$\begin{aligned} \left(\tfrac{\omega}{c}\right)^2 \tilde{F}_{\varphi 1,k} = \quad & \alpha_{11,k,0}\tilde{F}_{\varphi 1,k} + \alpha_{12,k,0}\tilde{F}_{\varphi 2,k} \\ & + \alpha_{12,k,1}\tilde{F}_{\varphi 2,k\pm 1} + \alpha_{12,k,2}\tilde{F}_{\varphi 2,k-J} \end{aligned} \qquad (14)$$

$$\begin{aligned} \left(\tfrac{\omega}{c}\right)^2 \tilde{F}_{\varphi 2,k} = \quad & \alpha_{22,k,0}\tilde{F}_{\varphi 2,k} + \alpha_{21,k,0}\tilde{F}_{\varphi 1,k} \\ & + \alpha_{21,k,1}\tilde{F}_{\varphi 1,k\mp 1} + \alpha_{21,k,2}\tilde{F}_{\varphi 1,k+J} \end{aligned} \qquad (15)$$

Figure 18 shows a schematic representation of the relation expressed in (14) and (15).

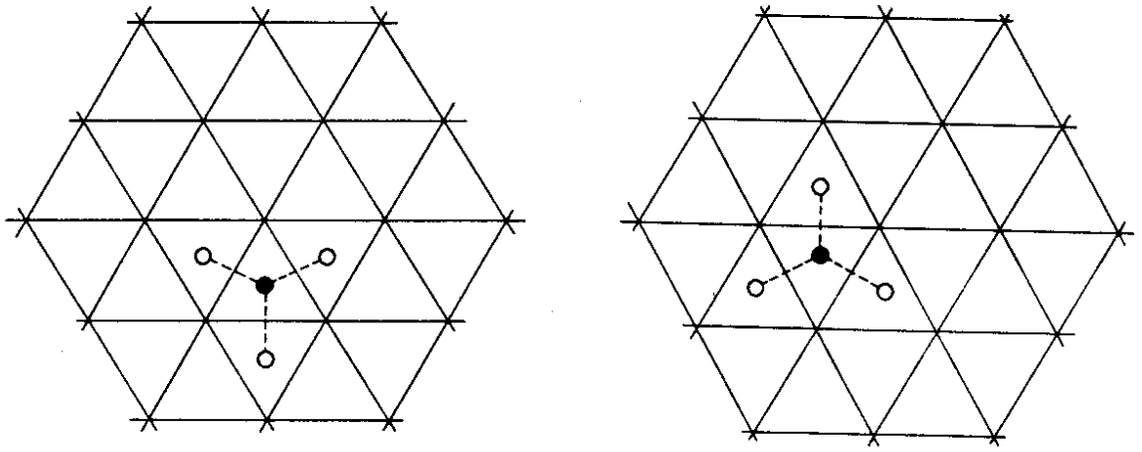

Figure 18 Connection of $\tilde{F}_{\varphi 1}$ and $\tilde{F}_{\varphi 2}$ to three neighbours by the difference equations

As for $m > 0$ a linear eigenvalue problem (13) is to be solved. The eigenvectors are now

$$\vec{x} = (\tilde{F}_{\varphi 1,1}, \ldots, \tilde{F}_{\varphi 1,N}, \tilde{F}_{\varphi 2,1}, \ldots, \tilde{F}_{\varphi 2,N})^T.$$

The 2N x 2N - matrix A is sparse, can be made symmetric and has only some off-diagonals(see figure 19).

$$\begin{pmatrix} A_{11} & A_{12} \\ A_{21} & A_{22} \end{pmatrix}$$

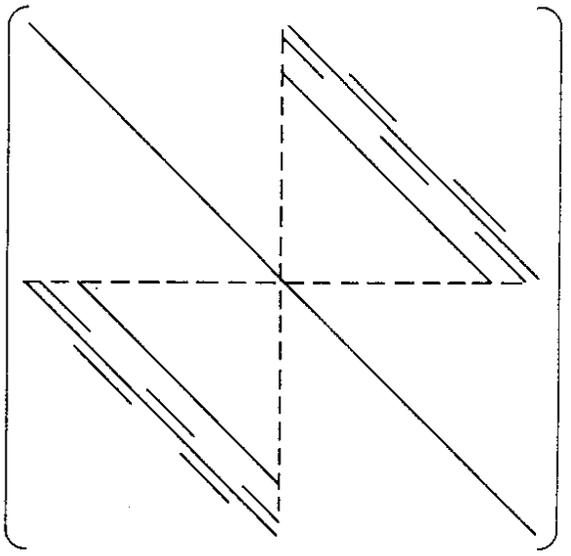

Figure 19 Matrix of the eigenvalue problem for $m = 0$

2.5 Waveguides and cavities of translational symmetry. The difference equations for the waveguide problem are similar to those for the deflecting modes. Instead of a certain azimuthal dependence we have the longitudinal dependance

$$\vec{E}(x, y, \Delta z) = \vec{E}_0(x, y)e^{i\beta\Delta z} \tag{16}$$

which is in first approximation

$$\vec{E}_0(x, y)(1 + i\beta\Delta z) \tag{17}$$

with the propagation constant β. The same is true for cavities that are not cylindrically symmetric but don't change their geometry in z-direction for $0 \leq z \leq L$ where L is the longitudinal length of the cavity.

Again Maxwell's equations are written in integral form and discretized in full analogy to the case of deflecting modes (compare appendix) with $(\vec{F}', \tilde{\vec{F}}')=(\vec{E}', \vec{B}')$. Then all $\vec{B}'$-components and the longitudinal $\vec{E}'$-component E_z are eliminated . The resulting linear algebraic eigenvalue problem has the squared propagation constants for a given frequency ω as eigenvalues.

This option of URMEL-T renders it possible to compute the functional relationship between the frequency and the propagation constant for e.g. dielectric loaded waveguides.

3. SOLUTION OF THE EIGENVALUE PROBLEM

We use the same method as in URMEL [**7**], [**8**], [**9**]. Since we are only interested in the n lowest eigenvalues the problem can be solved using a basis transformation which leads to a much smaller dimensional problem. The matrix of this problem acts over the subspace spanned by the n eigenvectors of the n lowest eigenvalues. This small eigenvalue problem is then solved by a direct conventional method (e.g. EISPACK-routine, [**6**]).

4. EXAMPLES

We will present calculations for several realistic cavities and waveguides with and without material insertions. To check the accuracy we consider first the pillbox cavity and a spherical cavity where we compare the results of URMEL-T with analytically calculated frequencies and with the results of URMEL.

4.1 Pillbox cavity and sphere. A detailed error analysis is not given here because of its extent. Besides the fineness of the mesh the quality of the approximation of the cavity geometry influences the error and this quality depends heavily on the given cavity.

To get an idea of the magnitude we choose the pillbox cavity for which no error due to the approximation of the geometry occurs and for which the exact resonance frequencies are analytically known. We compared an URMEL-run with N_1 points with an URMEL-T-run with N_2 points where $2N_1$ and $3N_2$ have about the same magnitude (because URMEL-T has three field values associated with each mesh point, while URMEL has two) for the calculation of deflecting modes (compare 2.3 respectively [**9**]). These runs used single precision, which gives on IBM about seven decimal digits. It is obvious that the rounding errors overcome the better discretization at some point. If very accurate results are needed the code can be run in double precision where the influence of rounding errors is much smaller.

Table 1 Lowest transverse mode frequencies in a pillbox of radius 1m and gap length 2m

	anal.,[**3**]	URMEL			URMEL-T		
mode	f / MHz	$2N_1$	f / MHz	error	$3N_2$	f / MHz	error
TM110	182.82	242	182.17	$-3.6 \cdot 10^{-3}$	216	182.43	$-2.1 \cdot 10^{-3}$
		968	182.67	$-8.2 \cdot 10^{-4}$	864	182.73	$-4.9 \cdot 10^{-4}$
		2178	182.76	$-3.3 \cdot 10^{-4}$	1944	182.76	$-3.3 \cdot 10^{-4}$
		3872	182.79	$-1.6 \cdot 10^{-4}$	3348	182.77	$-3.7 \cdot 10^{-4}$
		6050	182.76	$-3.3 \cdot 10^{-4}$	5016	182.73	$-4.9 \cdot 10^{-4}$
TE110	173.74	6050	173.67	$-4.0 \cdot 10^{-4}$	5016	173.72	$-1.2 \cdot 10^{-4}$

Double precision runs lead to the following relationship between accuracy and the number of mesh points:

$$\left| \frac{\Delta f}{f} \right| \sim \frac{1}{2.2 \cdot N^{1.2}} \tag{18}$$

The dependence of the error upon the number of unknown quantities is also illustrated in figure 20 for URMEL-T as well as for URMEL.

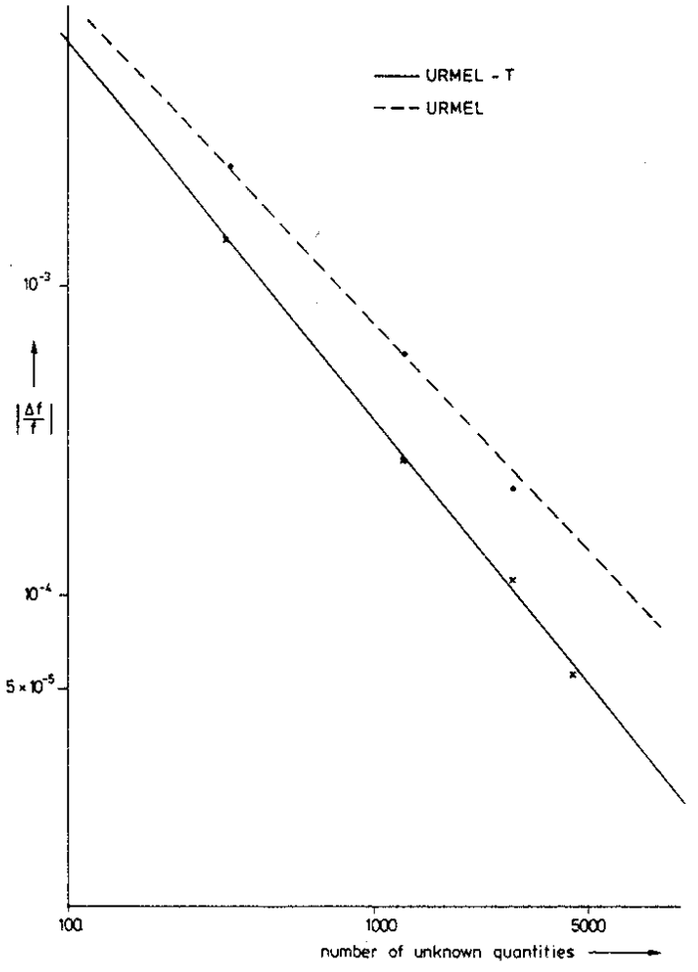

Figure 20 Relative error of the frequency in dependence upon the number of unknowns

For the spherical cavity a comparison of URMEL and URMEL-T makes evident the influence that the quality of the geometrical approximation has. This influence obviously depends on the special mesh used. Here we compared an URMEL-run with N_1 points with an URMEL-T-run with N_2 points where N_1 and $2N_2$ have about the same magnitude because URMEL-T has two azimuthal field values per mesh point while URMEL has one for the calculation of monopole modes (compare 2.4 respectively [**9**]).

Table 2 Lowest mode in a spherical cavity of radius 1m. Due to the spherical symmetry the mode EE1 with the exact frequency 130.911 MHz ([3]) can be calculated as TM0-EE-1 or as 1-ME-1; compare [9] for mode notation

		URMEL			URMEL-T	
mode	N	f / MHz	error	2N	f / MHz	error
TM0-EE-1	121	128.972	$-1.5 \cdot 10^{-2}$	144	130.750	$-1.2 \cdot 10^{-3}$
	484	130.733	$-1.4 \cdot 10^{-3}$	576	130.879	$-2.4 \cdot 10^{-4}$
	1089	130.762	$-1.1 \cdot 10^{-3}$	1296	130.892	$-1.5 \cdot 10^{-4}$
	1936	130.655	$-2.0 \cdot 10^{-3}$	2232	130.885	$-2.0 \cdot 10^{-4}$
	3025	130.721	$-1.5 \cdot 10^{-3}$	3510	130.929	$+1.4 \cdot 10^{-4}$

4.2 Dielectric loaded cavity. A new feature that URMEL-T offers is the possibility to insert dielectrics in the cavity. To investigate the accuracy of the program referring to this subject we examined the frequency shift caused by a piece of Teflon in a DORIS-cavity which has been measured.

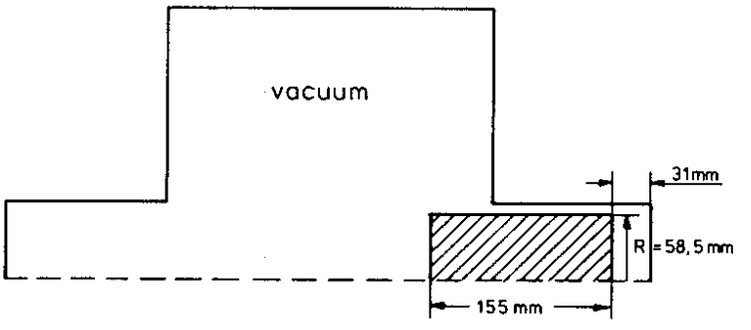

Figure 21 Dielectric loaded cavity

The DORIS-cavity with the inserted small Teflon cylinder is shown in figure 21. The computed frequency shift caused by this Teflon cylinder (dielectric constant $\epsilon_r = 2$) shows a good agreement with the measured data [13]. The reasonable difference found is due to the slightly modified cavity shape taken for the URMEL-T calculation where the flanges are left out.

Table 3 Frequency shift by a small Teflon cylinder inserted in a DORIS-cavity (N=968)

mode	calculated original frequency	measured original frequency	calculated frequency shift	measured frequency shift
TM010	498.406 MHz	498.488 MHz	6.356 MHz	6.614 MHz
TM011	739.302 MHz	745.667 MHz	7.419 MHz	8.399 MHz
TM110	775.286 MHz	775.870 MHz	4.606 MHz	5.980 MHz

4.3 Waveguide. For a dielectric waveguide we computed the relation between the frequency ω and the propagation constant β. The highest β's have been computed with URMEL-T for different frequencies. The result is illustrated in figure 22, which fits a few douzen distinct values of $k_0 (= \frac{\omega}{c})$ each representing a different URMEL-T run.

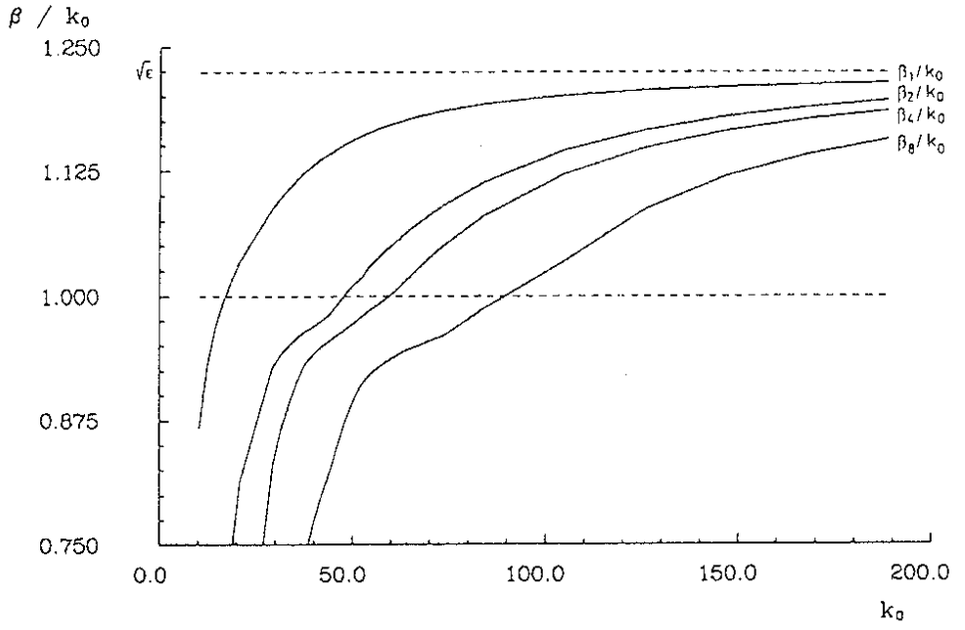

Figure 22 Relation between the wave number k_0 ($k_0 = \frac{\omega}{c}$) and $\frac{\beta}{k_0}$ for the dielectric loaded waveguide

Figure 23 shows a cut through the dielectric waveguide together with a possible triangular mesh. The corresponding transverse fields for the fundamental mode with frequency 3 GHz are plotted in figure 24.

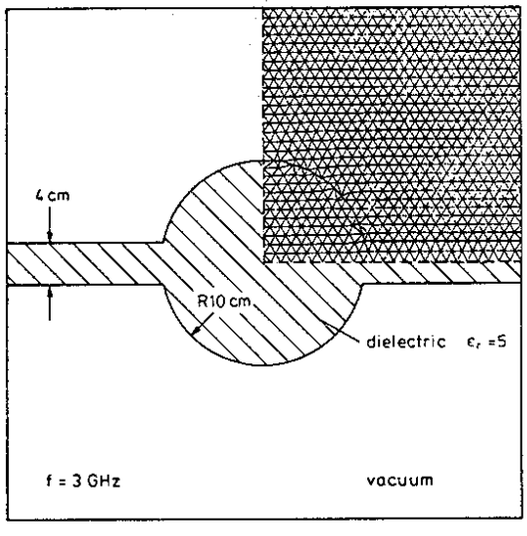

Figure 23 Dielectric waveguide with mesh for the part which is essential for a run of URMEL-T

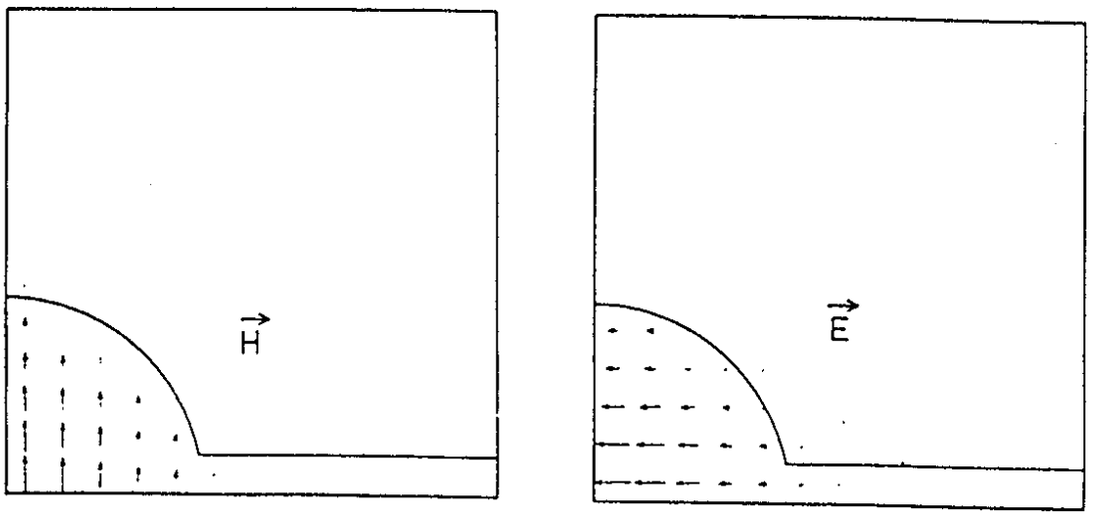

Figure 24 Field maps for the fundamental mode

4.4 A multi-cell cavity. To simulate the influence of the beam pipe it is usual to tune the last cell of a multi-cell cavity: The radius of this cell is modified to achieve a uniform field distibution in all cells. The triangular mesh is able to follow even very small deviations between the radii of the middle cells and the outer cell while a rectangular mesh needs to be very closely spaced to allow the representation of such an input geometry and to fulfill stability requirements. This causes a steeply increasing number of mesh points in rectangular grids for small changes in the radii of only a part of the cells, whereas for the triangular mesh the mesh size may be left unchanged.

To illustrate this fact we show the tuned 1GHz PETRA nine-cell superconducting cavity. The radius of the middle cells is 139.595 mm while the last cell has a radius of 138.345 mm. Figure 25 shows the cavity together with the triangular mesh of 1960 points. To approximate this geometry in a rectangular mesh many more points would be necessary. Figure 26 shows contours of $r \cdot H_\varphi = const$ of the π mode. These lines show the direction of the electric field. Their density is proportional to $r \cdot \vec{E}$. An arrow plot of the electric field of this mode is also shown in figure 27. The countours of constant $r \cdot H_\varphi$ of an higher monopole mode can be seen in figure 28. Figures 29, 30 and 31 present arrow plots of the electric respectively magnetic field of two Dipol modes. The calculates frequencies are compared with measured frequencies [5]. The measurements have been done with a cavity with only very small differences in the cavity shape.

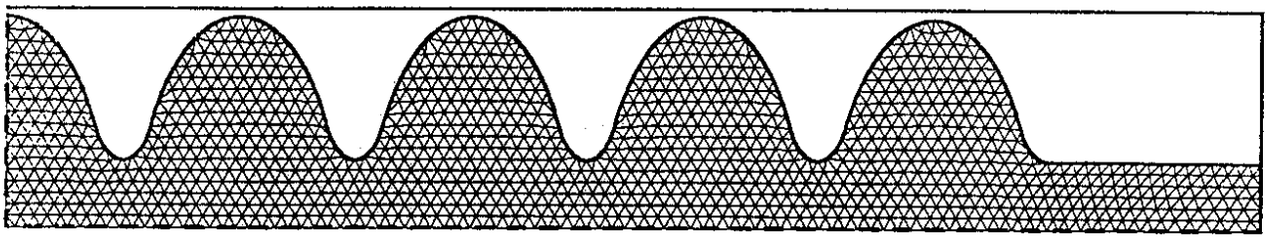

Figure 25 Tuned PETRA nine cell cavity with mesh used

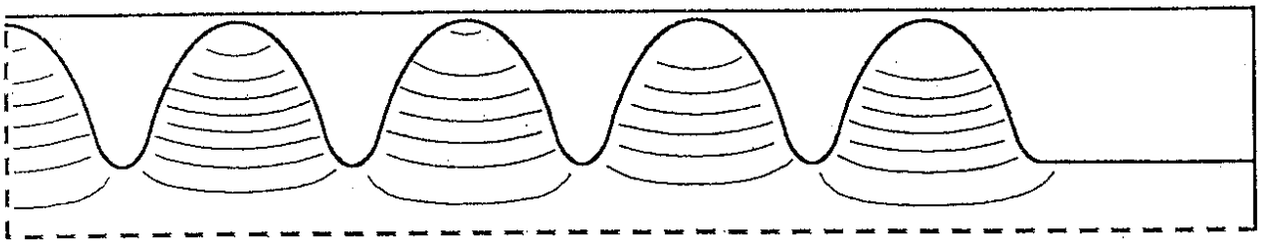

Figure 26 Contours of constant $r \cdot H_\varphi$ for the π-mode of the tuned nine cell cavity

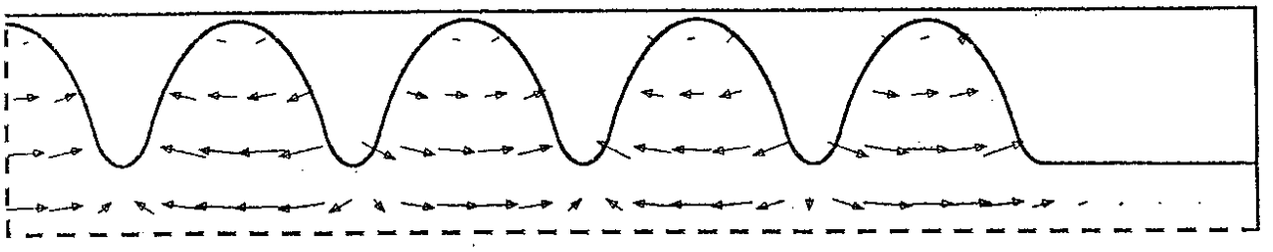

Figure 27 Arrow plot of the electric field for the π-mode.
The measurements gave 1000.1 MHz as frequency, URMEL-T calculated 1007.5 MHz.

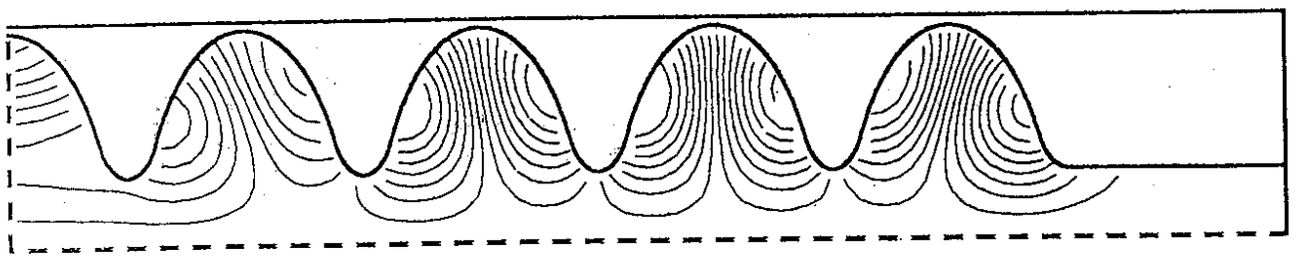

Figure 28 Contours of constant $r \cdot H_\varphi$ for the TM011-$8\pi/9$-mode.
The measurements gave 1983.7 MHz as frequency, URMEL-T calculated 1975.3 MHz.

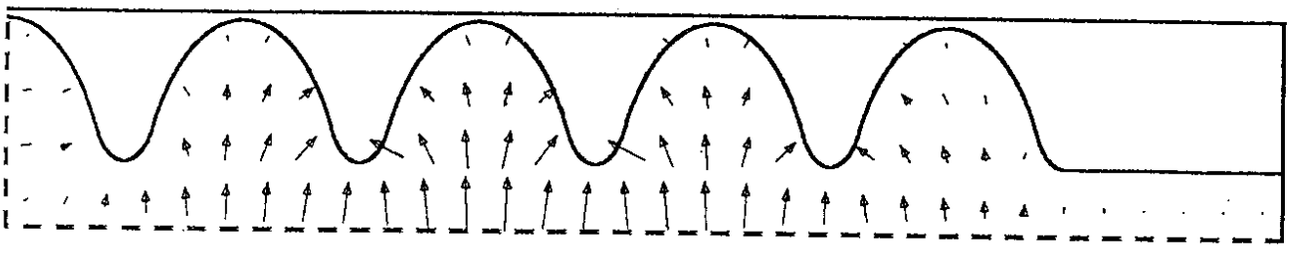

Figure 29 Arrow plot of the electric field for the "TE111-$2\pi/9$"-like mode.
The measurements gave 1271.2 MHz as frequency, URMEL-T calculated 1289.8 MHz.

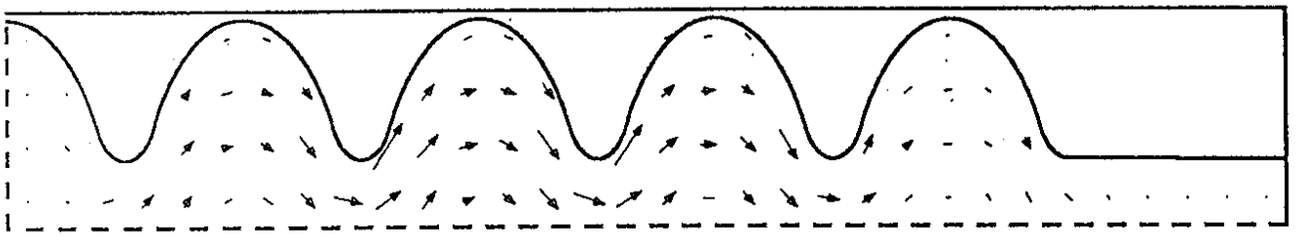

Figure 30 Arrow plot of the magnetic field for the "TE111-$2\pi/9$"-like mode.

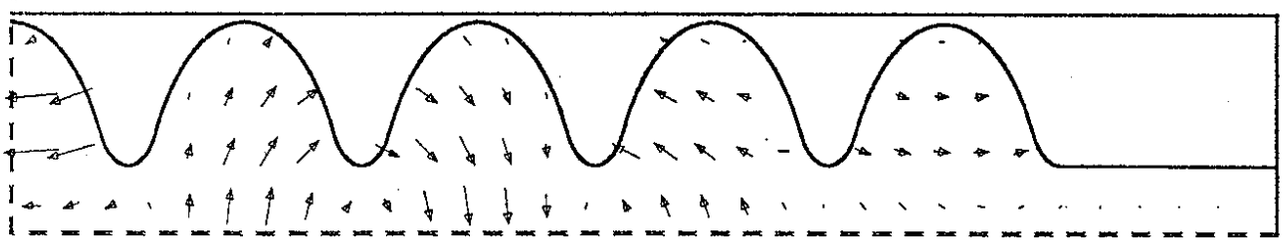

Figure 31 Arrow plot of the electric field for the "TM110-$\pi/9$"-like mode.
The measurements gave 1428.7 MHz as frequency. URMEL-T calculated 1432.7 MHz.

5. The Program

The code of URMEL-T is available at DESY. The structure of the input data is compatible with that of URMEL. For the features that URMEL-T offers in addition some new parameters have been introduced. The interface routines (e.g. for plotting) are the same as for URMEL and TBCI [**10**] so that the code can be installed easily. More detailed information about the program is given in the user's guide [**4**].

6. Summary

The computer code URMEL-T enlarges the two dimensional scope of application of the FIT-discretization method in two directions:

- First it allows the calculation of resonant modes (including the TE0-modes) in cylindrically or translationally symmetric cavities with dielectric and/or permeable insertions as well as the calculation of propagation constants in waveguides.
  Herewith URMEL-T offers a new feature in the domain of computational evaluation of RF-fields.
- Second URMEL-T is well suited to structures with elliptical or circular parts in their geometry, and for tuning multi-cell cavities. This is based on the properties of a triangular mesh combined with the powerful FIT-method. The latter makes sure that the solutions fulfill all Maxwell's equations, i.e. they are physically significant.

So URMEL-T presents a widely useful extension of the program group for the solution of Maxwell's equations.

7. APPENDIX

The discretization of Maxwell's equations (9) is shown in this chapter. The derivation of the difference equations includes the incorporation of the boundary conditions. To elucidate the principle it is sufficient to consider the case $(\vec{F}', \vec{\tilde{F}}')=(\vec{E}', \vec{B}')$.

7.1 Integration for $E_{a,k}$, $E_{b,k}$ and $E_{c,k}$. We integrate

$$\oint \vec{H}' \cdot d\vec{s} = k \int \epsilon_r \vec{E}' \cdot d\vec{A}$$

over the area shown in figure 32 (for cavities) or figure 33 (for waveguides).

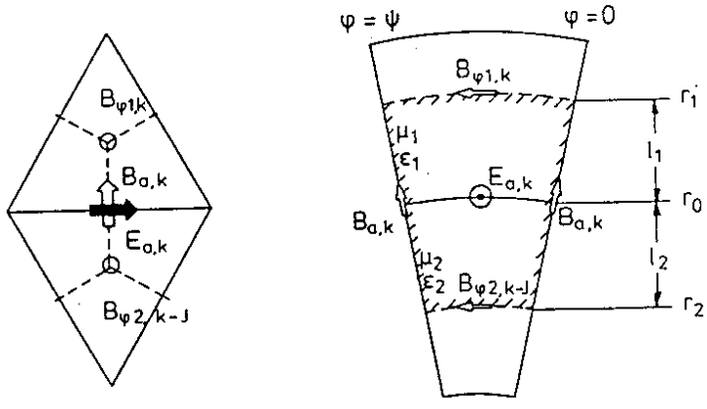

Figure 32 Area of integration for $E_{a,k}$: cavities

The left-hand figure is the mesh drawn in a plane φ =const, while the right-hand figure is in the plane used for the integration of $E_{a,k}$.

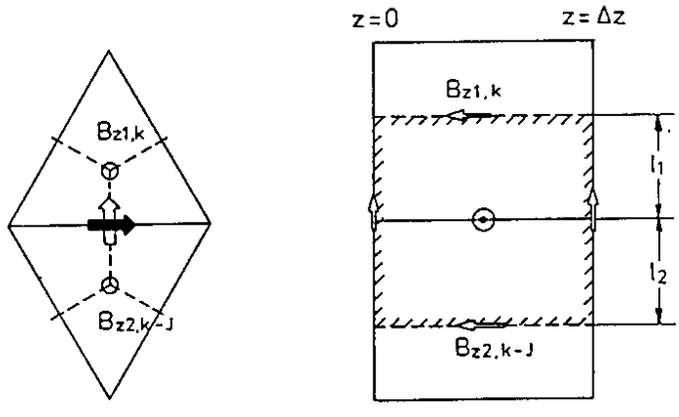

Figure 33 Area of integration for $E_{a,k}$: waveguides

The left-hand figure is drawn in a plane z =const, while the right-hand figure is in the plane used for the integration of $E_{a,k}$.

(a) Cavities

$$k \cdot E_{a,k} \cdot cos\alpha_k \cdot (\epsilon_{1,k} \cdot \pi \cdot l_1 \cdot (r_0 + r_1) + \epsilon_{2,k-J} \cdot \pi \cdot l_2 \cdot (r_0 + r_2)) \cdot \int_0^{\psi} \frac{\cos m\varphi}{2\pi} d\varphi$$
$$= (B_{\varphi 1,k} \cdot \frac{2\pi r_1}{\mu_{1,k}} - B_{\varphi 2,k-J} \cdot \frac{2\pi r_2}{\mu_{2,k-J}}) \cdot \int_0^{\psi} \frac{\cos m\varphi}{2\pi} d\varphi$$
$$- B_{a,k} \cdot \left(\frac{l_1}{\mu_{1,k}} + \frac{l_2}{\mu_{2,k-J}} \right) \cdot \sin m\psi, \quad (19)$$

with $0 < \psi \leq 2\pi$, and α_k is the angle between $E_{a,k}$ and the normal to the plane used for the integration.
Thus we have an equation of the form, letting $\psi \to 0$,

$$kE_{a,k} = a_{1,k}B_{\varphi 1,k} - a_{2,k}B_{\varphi 2,k-J} - ma_{3,k}B_{a,k} \quad (20)$$

with formal coefficients $a_{1,k}, a_{2,k}$ and $a_{3,k}$. In the same way we get linear equations for $E_{b,k}$ and $E_{c,k}$:

$$kE_{b,k} = b_{1,k}B_{\varphi 1,\,{}^{k-1}_{k}} - b_{2,k}B_{\varphi 2,k} + mb_{3,k}B_{b,k}, \quad (21)$$
$$kE_{c,k} = -c_{1,k}B_{\varphi 1,k} + c_{2,k}B_{\varphi 2,\,{}^{k}_{k-1}} + mc_{3,k}B_{c,k}, \quad (22)$$

where the superposed subscripts indicate values to be used for mesh points of type I or II, respectively (upper=type I; compare section 2.1 and figure 11).

(b) Waveguides
To first order in Δz, and where α_k is the angle between $E_{a,k}$ and the normal to the integration-plane,

$$i \cdot k \cdot E_{a,k} \cdot cos\alpha_k \cdot (\epsilon_{1,k} \cdot \Delta z \cdot l_1 + \epsilon_{2,k-J} \cdot \Delta z \cdot l_2)$$
$$= (B_{z1,k} \cdot \frac{1}{\mu_{1,k}} - B_{z2,k-J} \cdot \frac{1}{\mu_{2,k-J}}) \cdot \Delta z$$
$$- B_{a,k} \cdot \left(\frac{l_1}{\mu_{1,k}} + \frac{l_2}{\mu_{2,k-J}} \right) \cdot i \cdot \beta \cdot \Delta z. \quad (23)$$

This gives, letting $\Delta z \to 0$, an equation of the form

$$ikE_{a,k} = a_{1,k}B_{z1,k} - a_{2,k}B_{z2,k-J} - i\beta a_{3,k}B_{a,k}. \quad (24)$$

Likewise we get for $E_{b,k}$ and $E_{c,k}$:

$$ikE_{b,k} = b_{1,k}B_{z1,\,{}^{k-1}_{k}} - b_{2,k}B_{z2,k} + i\beta b_{3,k}B_{b,k}, \quad (25)$$
$$ikE_{c,k} = -c_{1,k}B_{z1,k} + c_{2,k}B_{z2,\,{}^{k}_{k-1}} + i\beta c_{3,k}B_{c,k}, \quad (26)$$

where again the superposed subscripts denote values to be used depending to the row of the mesh being considered.

7.2 Integration for $B_{a,k}$, $B_{b,k}$, $B_{c,k}$, $B_{\varphi 1,k}$ and $B_{\varphi 2,k}$. The Maxwell equation

$$\oint \vec{E}' \cdot d\vec{s} = k \int \mu_r \vec{H}' \cdot d\vec{A}$$

is integrated over the areas shown in figures 34 (respectively 35) and in figure 36.

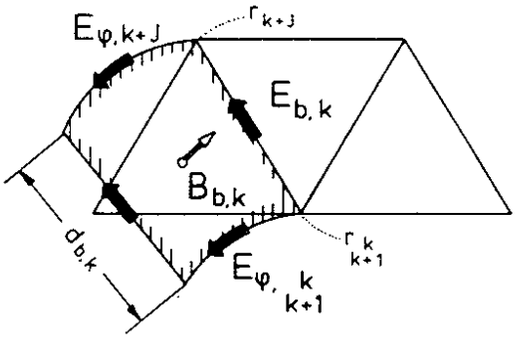

Figure 34 Area of integration for $B_{b,k}$; cavities

The shaded path is perpendicular to the triangular mesh and results from sweeping the mesh through an angle ψ about the z-axis.

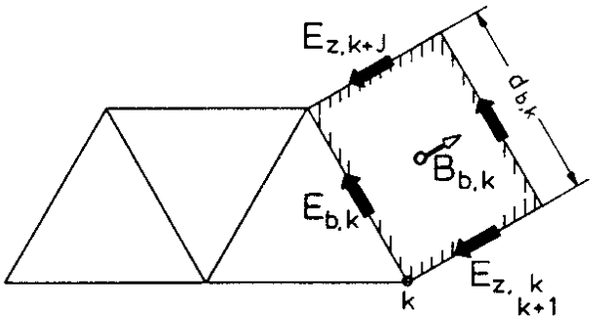

Figure 35 Area of integration for $B_{b,k}$; waveguides

The shaded path is perpendicular to the triangular mesh and results from sweeping the mesh through a distance Δz along the z axis.

For $B_{b,k}$ we get

(a) Cavities

$$k \cdot B_{b,k} \cdot cos\beta_k \cdot \pi(r_{\frac{k}{k+1}} + r_{k+J}) \cdot d_{b,k} \cdot \int_0^{\psi} \frac{\sin m\varphi}{2\pi} d\varphi$$
$$= (-E_{\varphi,\frac{k}{k+1}} \cdot 2\pi \cdot r_{\frac{k}{k+1}} + E_{\varphi,k+J} \cdot 2\pi \cdot r_{k+J}) \cdot \int_0^{\psi} \frac{\sin m\varphi}{2\pi} d\varphi$$
$$+ E_{b,k} \cdot d_{b,k} \cdot (\cos m\psi - 1), \quad (27)$$

with $0 < \psi \leq 2\pi$. This gives

$$kB_{b,k} = -e_{1,k}E_{\varphi,\frac{k}{k+1}} + e_{2,k}E_{\varphi,k+J} + me_{3,k}E_{b,k}. \quad (28)$$

The integration area is shown in figure 34. Analogously the equations for $B_{a,k}$ and $B_{c,k}$ are:

$$kB_{a,k} = d_{1,k}E_{\varphi,k} - d_{2,k}E_{\varphi,k+1} - md_{3,k}E_{a,k}, \quad (29)$$
$$kB_{c,k} = f_{1,k}E_{\varphi,\frac{k+J+1}{k+J}} - f_{2,k}E_{\varphi,k} + mf_{3,k}E_{c,k}. \quad (30)$$

(b) Waveguides
To first order in Δz

$$-i \cdot k \cdot B_{b,k} \cdot cos\beta_k \cdot \Delta z \cdot d_{b,k}$$
$$= (-E_{z,\frac{k}{k+1}} + E_{z,k+J}) \cdot \Delta z + E_{b,k} \cdot d_{b,k} \cdot i \cdot \beta \cdot \Delta z. \quad (31)$$

Hence, letting $\Delta z \to 0$,

$$-ikB_{b,k} = -e_{1,k}E_{z,\frac{k}{k+1}} + e_{2,k}E_{z,k+J} + i\beta e_{3,k}E_{b,k}. \quad (32)$$

The integration area is shown in figure 35. Analogously the equations for $B_{a,k}$ and $B_{c,k}$ are:

$$-ikB_{a,k} = d_{1,k}E_{z,k} - d_{2,k}E_{z,k+1} - i\beta d_{3,k}E_{a,k}, \quad (33)$$
$$-ikB_{c,k} = f_{1,k}E_{z,\frac{k+J+1}{k+J}} - f_{2,k}E_{z,k} + i\beta f_{3,k}E_{c,k}. \quad (34)$$

In order to eliminate the azimuthal (respectively longitudinal) $\vec{B}'$-components we integrate this Maxwell-equation over one mesh cell as illustrated in figure 36.

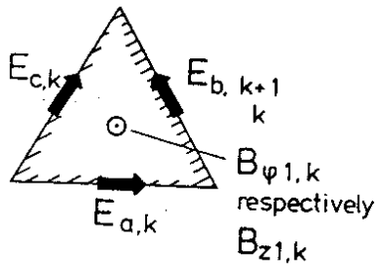

Figure 36 Area of integration for $B_{\varphi 1,k}$ respectively $B_{z1,k}$

(a) Cavities

$$k \cdot A_{1,k} \cdot B_{\varphi 1,k} = E_{a,k} \cdot d_{a,k} + E_{b,\,k}^{\,k+1} \cdot d_{b,\,k}^{\,k+1} - E_{c,k} \cdot d_{c,k}. \tag{35}$$

Thus we get

$$kB_{\varphi 1,k} = g_{1,k}E_{a,k} + g_{2,k}E_{b,\,k}^{\,k+1} - g_{3,k}E_{c,k}, \tag{36}$$

$$kB_{\varphi 2,k} = h_{1,k}E_{c,\,k+1}^{\,k} - h_{2,k}E_{a,k+J} - h_{3,k}E_{b,k}. \tag{37}$$

(b) Waveguides

$$-i \cdot k \cdot A_{1,k} \cdot B_{z1,k} = E_{a,k} \cdot d_{a,k} + E_{b,\,k}^{\,k+1} \cdot d_{b,\,k}^{\,k+1} - E_{c,k} \cdot d_{c,k}. \tag{38}$$

This gives

$$-ikB_{z1,k} = g_{1,k}E_{a,k} + g_{2,k}E_{b,\,k}^{\,k+1} - g_{3,k}E_{c,k}, \tag{39}$$

$$-ikB_{z2,k} = h_{1,k}E_{c,\,k+1}^{\,k} - h_{2,k}E_{a,k+J} - h_{3,k}E_{b,k}. \tag{40}$$

With these equations we can substitute all magnetic quantities in the equations (20)-(22) or else (24)-(26).

7.3 Integration for E_φ respectively E_z. Finally we want to get a relation between E_φ or E_z and the other electric field components. Since the third Maxwell equation

$$\iint \epsilon_r \vec{E}' \cdot d\vec{A} = 0$$

is automatically fulfilled for time-harmonic fields in the FIT-method [**11**] we will use this one to obtain the desired relation.

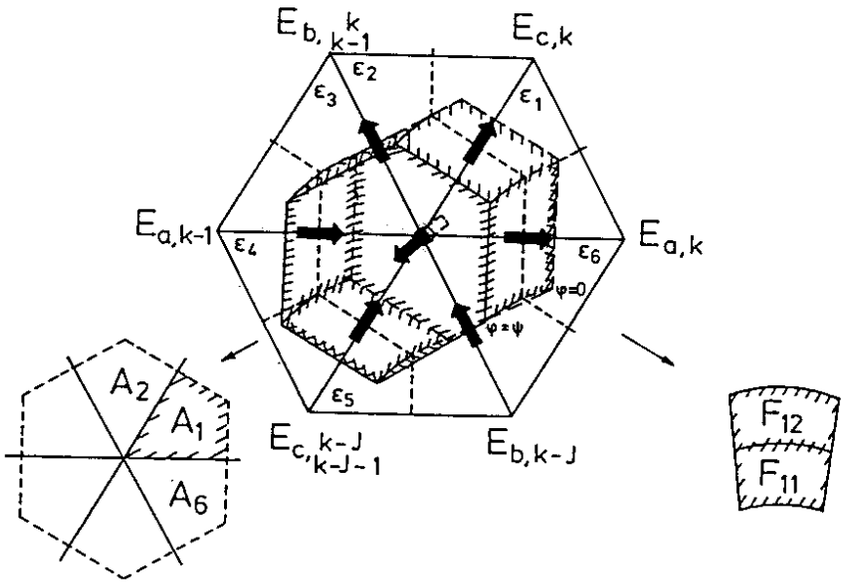

Figure 37 Area of integration for $E_{\varphi,k}$ respectively $E_{z,k}$

This equation is integrated over the surface shown in figure 37 and leads to

$$\begin{aligned}
&E_{\varphi,k}\cdot(\epsilon_1A_1+\epsilon_2A_2+\cdots+\epsilon_6A_6)\sin m\psi\\
&+E_{a,k}\cdot(\epsilon_6F_{11}+\epsilon_1F_{12})\int_0^\psi\cos m\varphi\,d\varphi \qquad +E_{c,k}\cdot(\epsilon_1F_{21}+\epsilon_2F_{22})\int_0^\psi\cos m\varphi\,d\varphi \qquad (41)\\
&+E_{b,\,k-1}^{\,k}\cdot(\epsilon_2F_{31}+\epsilon_3F_{32})\int_0^\psi\cos m\varphi\,d\varphi \qquad -E_{a,k-1}\cdot(\epsilon_3F_{41}+\epsilon_4F_{42})\int_0^\psi\cos m\varphi\,d\varphi\\
&-E_{c,\,k-J-1}^{\,k-J}\cdot(\epsilon_4F_{51}+\epsilon_5F_{52})\int_0^\psi\cos m\varphi\,d\varphi \qquad -E_{b,k-J}\cdot(\epsilon_5F_{61}+\epsilon_6F_{62})\int_0^\psi\cos m\varphi\,d\varphi=0
\end{aligned}$$

respectively

$$\begin{aligned}
&i\cdot\beta\cdot E_{z,k}\cdot(\epsilon_1A_1+\epsilon_2A_2+\cdots+\epsilon_6A_6)\cdot\Delta z\\
&+E_{a,k}\cdot(\epsilon_6F_{11}+\epsilon_1F_{12})\cdot\Delta z \qquad +E_{c,k}\cdot(\epsilon_1F_{21}+\epsilon_2F_{22})\cdot\Delta z \qquad (42)\\
&+E_{b,\,k-1}^{\,k}\cdot(\epsilon_2F_{31}+\epsilon_3F_{32})\cdot\Delta z \qquad -E_{a,k-1}\cdot(\epsilon_3F_{41}+\epsilon_4F_{42})\cdot\Delta z\\
&-E_{c,\,k-J-1}^{\,k-J}\cdot(\epsilon_4F_{51}+\epsilon_5F_{52})\cdot\Delta z \qquad -E_{b,k-J}\cdot(\epsilon_5F_{61}+\epsilon_6F_{62})\cdot\Delta z \qquad =0
\end{aligned}$$

which gives the following relation

$$mE_{\varphi,k}=-l_{1,k}E_{a,k}-l_{2,k}E_{c,k}-l_{3,k}E_{b,\,k-1}^{\,k}+l_{4,k}E_{a,k-1}+l_{5,k}E_{c,\,k-J-1}^{\,k-J}+l_{6,k}E_{b,k-J} \qquad (43)$$

respectively

$$i\beta E_{z,k}=-l_{1,k}E_{a,k}-l_{2,k}E_{c,k}-l_{3,k}E_{b,\,k-1}^{\,k}+l_{4,k}E_{a,k-1}+l_{5,k}E_{c,\,k-J-1}^{\,k-J}+l_{6,k}E_{b,k-J} \qquad (44)$$

Using this relation we finally get (10)-(12).

REFERENCES

1. A.G. Daikovsky, Yu.I. Portugalov, A.D. Ryabov, *PRUD-Code for Calculation of the Non-symmetric Modes in Axial Symmetric Cavities*, Particle Accelerators **12** (1982), 59–64.

2. K. Halbach, R.F. Holsinger, *SUPERFISH - A computer program for evaluation of rf cavities with cylindrical symmetry*, Particle Accelerators **7** (1976), 213–222.

3. H. Henke, *Spherical modes*, CERN-ISR-RF/81-29, August 1981.

4. C. Palm, U. van Rienen, T. Weiland, *URMEL and URMEL-T Userguide (Modal Analysis of Cylindrically Symmetric Cavities; Evaluation of RF-Fields in Waveguides)*, DESY M-85-11, October 1985.

5. J. Peters, T. Weiland, *Mode Computation and Measurement of the DESY Nine Cell Superconducting Cavity*, DESY M-85-02, February 1985.

6. B.T. Smith et al., "Matrix Eigensystem Routines - EISPACK Guide", Springer-Verlag, Berlin Heidelberg New York, 1976.

7. J. Tückmantel, *URMEL 1.8, URMEL with a high speed and high precision eigenvector finder*, CERN/EF/RF 83-5, July 1983.

8. J. Tückmantel, *Application of SAP in URMEL*, CERN/EF/RF 85-4, July 1985.

9. T. Weiland, *On the computation of resonant modes in cylindrically symmetric cavities*, Nuclear Instruments and Methods NIM **216** (1983), 329–348.

10. T. Weiland, *On the numerical solution of Maxwell's equations and applications in the field of accelerator physics*, Particle Accelerators **15** (1984), 245–292 and references therein.

11. T. Weiland, *Eine Methode zur Lösung der Maxwellschen Gleichungen für sechskomponentige Felder auf diskreter Basis*, AEÜ Archiv für Elektronik und Übertragungstechnik **31** (1977), 116–120.

12. T. Weiland, *Design of RF Quadrupoles and RF Waveguides with URMEL 3.0*, DESY HERA 84-18, August 1984.

13. A. Zolfaghari, private communication.

LIST OF SYMBOLS

$\vec{E}, \vec{H}$	electric and magnetic field
$\vec{F}, \vec{\tilde{F}}$	field on the triangular and on the dual mesh
$F_{a,k}$	projection of the $\vec{F}$ - field on the triangle side a attached to mesh node k
$\tilde{F}_{\varphi i,k}$	azimuthal $\vec{\tilde{F}}$ - field component at triangle i of node $k; i = 1,2$
Z_0, Y_0	free space impedance, admittance
ϵ_0	permittivity of the vacuum, $\frac{10^7}{4\pi c^2}$
μ_0	permeability of the vacuum, $4\pi \cdot 10^{-7}$
c	speed of light
ϵ_r	relative permittivity; material constant $\frac{\epsilon}{\epsilon_0}$
μ_r	relative permeability; material constant $\frac{\mu}{\mu_0}$
m	azimuthal mode number,i.e. fields $\propto \cos m\varphi$ resp. $\sin m\varphi$
1-EE-4	mode with electric boundary on both sides, dipole, 4-th mode found in this subset
2-ME-3	mode with magnetic boundary on the left and electric boundary on the right, quadrupole, third mode found in this subset
k	wave number, $k = \frac{\omega}{c}$
$\mathbf{G}$	triangular mesh
$\mathbf{G_M}$	dual mesh with perpendicular bisectors for sides
$\mathbf{G_S}$	dual mesh with centres of mass of each triangle as (dual) mesh points
i, j	running index for mesh lines/points in r,z (x,y) direction
I, J	number of mesh lines in r (x) direction, number of points (in z (y) direction) on each mesh line in r (x) direction
N	number of mesh points; $N = I \cdot J$
k	as index: mesh point number $k = (i-1) \cdot J + j$
$\alpha_{bc,k,p}$	element of A_{bc} where p is 0-3 denoting one of the diagonals
$\alpha_{12,k,p}$	element of A_{12} where p is 0-2 denoting one of the diagonals
A	matrix of the eigenvalue problem
A_{aa}	submatrix connecting F_a and F_a
A_{21}	submatrix connecting $\tilde{F}_{\varphi 2}$ and $\tilde{F}_{\varphi 1}$
$\vec{x}$	column vector holding all $\vec{F}$ resp. $\vec{\tilde{F}}$ field components
$\vec{e}_r, \vec{e}_\varphi, \vec{e}_z$	unit vector in r,φ ,z direction